



Controlled synthesis of 3D porous structured cobalt-iron based nanosheets by electrodeposition as asymmetric electrodes for ultra-efficient water splitting



Yu Pei^a, Yuancai Ge^a, Hang Chu^a, William Smith^b, Pei Dong^{b,c}, Pulickel M. Ajayan^c, Mingxin Ye^{a,*}, Jianfeng Shen^{a,c,*}

^a Institute of Special Materials and Technology, Fudan University, Shanghai, 200433, China

^b Department of Mechanical Engineering, George Mason University, Virginia, 22030, USA

^c Department of Materials Science and NanoEngineering, Rice University, 6100 Main Street, Houston, TX, 77005, USA

ARTICLE INFO

Keywords:

Electrodeposition
3D porous structure
CoFe-LDH/CoFe-P
Asymmetric electrodes
Water splitting

ABSTRACT

Exploring more active, low-cost and stable electrocatalysts to substitute precious noble metals has always been a research focus on the application of water splitting. In this study, firstly, we prepared CoFe-layered double hydroxide (CoFe-LDH) via one-step electrodeposition. The CoFe-LDH nanosheets grew on the nickel foam and formed a 3D hierarchical structure, making the CoFe-LDH exhibit excellent activity for oxygen evolution reaction (OER). The overpotential was 250 mV and the Tafel slope is 35 mV dec⁻¹ at 10 mA cm⁻² in alkaline condition. With such a 3D porous structure as a framework, we fabricated CoFe phosphides using a solid-phase reaction. After phosphorization, the nanosheets retained the original 3D porous structure and electrochemical performance for hydrogen evolution reaction had been greatly enhanced. The overpotential in alkaline condition was 58 mV and the Tafel slope is 46 mV dec⁻¹ at 10 mA cm⁻². The CoFe-LDH and CoFe-P with Ni foams were used as asymmetric electrodes for overall water splitting. At the potential of 1.51 V, this electrolysis apparatus can reach a current density of 10 mA cm⁻² in 1 M KOH, which is superior to all of the reported non-precious metal based ones.

1. Introduction

As the environmental issues and energy crisis become more serious, the development of new energy is the focus of current research. Hydrogen (H₂), as an efficient and environmentally energy, has great potential applications [1–7]. Currently, electrolysis of water is a very effective way to produce hydrogen [8–10]. This process is composed of two half reactions, the hydrogen evolution reaction (HER) and the oxygen evolution reaction (OER) [11,12]. In these two reactions, the catalyst can greatly reduce the energy barrier during the reaction. The most representative catalysts for water splitting are noble metal-based materials (e.g., Pt-based and Ir/Ru-based). Although these precious metal-based catalysts possess high catalytic activity, the high cost, poverty, single function and poor stability limit their widespread application [13–22]. To acquire more practical and efficient catalysts for large-scale applications, the catalysts should be prepared by common materials and method should be as simple as possible [23]. In the past few years, researchers have developed a variety of effective HER and

OER catalysts based on the transition metal-based compounds [24–27].

Recently, some common transition metal materials have been widely explored for use as either HER or OER electrocatalysts for electrochemical water splitting application [28–38]. Among OER catalysts, transition metal hydroxides (e.g., Co-OH, Ni-OH, NiFe-LDH, CoFe-LDH) have gained more and more attention for the abundance, high electrical conductivity and excellent electrochemical activity [39–47]. In these transition metal hydroxides, CoFe-LDH has displayed high catalytic activity for OER. The enhanced activity may owe to the formation of the O–O bond by breaking the Co–O bond [48]. There are two main methods for preparing bimetallic hydroxide, electrodeposition and hydrothermal method. Qiu et al. synthesized CoFe-LDH by hydrothermal method. This 2D nanosheet-shaped CoFe-LDH could be used as an efficient and stable oxygen evolution catalyst [49]. Huang et al. synthesized a series of bifunctional, 3D Ni-M (M = Fe, Co) LDH@NF with the excellent performances for overall water splitting through the hydrothermal method. The Ni₅Fe LDH@NF exhibited low overpotentials of 210 mV for OER [50]. Compared with the hydrothermal

* Corresponding authors at: Institute of Special Materials and Technology, Fudan University, Shanghai, 200433, China.

E-mail addresses: mxye@fudan.edu.cn (M. Ye), jfshen@fudan.edu.cn (J. Shen).

method, electrodeposition is more convenient, and the preparation process is simpler. The electrodeposited amorphous Co-Fe nanosheets show higher performance for OER with an overpotential of 280 and 295 mV @ 10 mA cm⁻² due to strong electronic interactions between Co and Fe [30,51]. The CoFe-LDH electrocatalyst by electrodeposition for OER have been reported in some publications. However, there are few studies on the influence of deposition time on morphology and electrochemical performance.

Although the bimetallic hydroxides have excellent OER performance, their HER performance is poor. Transition metal phosphides (TMPs) are a typical new type of highly efficient catalysts at present. More and more attentions have been given to TMPs due to their high HER activity [20,52–64]. Sun et al. fabricated self-supported Fe-doped Ni₂P nanosheets with NF by a simple hydrothermal method and in situ phosphorization. The optimized Fe doping of Ni₂P [(Ni_{0.33}Fe_{0.67})₂P] showed excellent HER performance. It requires only ~214 mV to reach a current density of 50 mA cm⁻² [65]. Li et al. synthesized cobalt phosphide-carbon nanotubes (CoP-CNTs) hybrids under mild conditions. The synthesized CoP-CNTs hybrids manifested superior activity for HER in 0.5 M H₂SO₄, which just required 139 mV @ 10 mA cm⁻² [66]. Paik et al. reported a facile template-engaged strategy to synthesize cubic quasi-hollow Ni–Co–P. The nickel cobalt phosphide nanocubes exhibited high activity for HER in 1 M KOH [67].

Herein, the CoFe-based electrocatalysts for water splitting were synthesized in two steps. First, we prepared CoFe-LDH nanosheets on Ni foam directly by electrodeposition, which can simplify the preparation of electrode materials, significantly reduce costs, and enhance activity with 3D morphology. We delved into the effects of deposition time. We also used FIB to study samples for the first time. CoFe-LDH exhibited excellent OER performance, which can reach current density of 10 mA cm⁻² with an overpotential of 250 mV and Tafel slope is 35 mV dec⁻¹. Based on 3D structured CoFe-LDH/NF electrodes, a bimetallic phosphide (CoFe-P/NF) electrode for HER was further fabricated via a facile method by using a one-step phosphorization. The CoFe-P/NF electrode maintains the nanosheet-like morphology after phosphorization. It exhibits high catalytic activity for HER in 1 M KOH. The CoFe-P/NF electrode only required an overpotential of 58 mV to reach the current density of 10 mA cm⁻² with the Tafel slope of 46 mV dec⁻¹. With both CoFe-LDH and CoFe-P electrocatalysts were successfully prepared, we constructed a highly efficient asymmetric electrolysis device by using CoFe-LDH and CoFe-P as anodes and cathodes respectively for the first time. At the work voltage of only 1.51 V, the current density could arrive 10 mA cm⁻².

2. Experimental

2.1. Materials

Hydrochloric acid (HCl), Cobaltous nitrate (Co(NO₃)₂·6H₂O), ferrous sulfate (FeSO₄·7H₂O) and sodium hypophosphite (NaH₂PO₂·H₂O) were obtained from Sinopharm Chemical Reagent Co., Ltd (SCRC).

2.2. Electrodeposition of CoFe-LDH on Ni foam

Scheme 1 displays the fabrication process of the electrocatalysts for water splitting. A facile electrodeposition method was used to prepare CoFe-LDH nanosheets. Before electrodeposition, Ni foam (thickness: 1 mm) was cleaned with 2 M HCl for 10 min to clean the oxide layer, then washed with ethanol and water. Then kept in air to ensure a clean surface. The electrodeposition process is performed under a three-electrode system. Pt wire was used as counter electrode and working electrode was Ni foam. Meanwhile, the reference electrode was calomel. The electrodeposited solution consisted of Co(NO₃)₂·6H₂O (0.15 M), FeSO₄·7H₂O (0.15 M) with DI water. An i-t program with potential of -1.0 V was used for electrodeposition. Different CoFe-LDH samples were fabricated by controlling the electrodeposition time (100,

200, and 400 s), which are herein labeled as CoFe-H-1, CoFe-H-2, and CoFe-H-4, respectively. The Co-H was prepared by the same electrochemical procedure without the FeSO₄·7H₂O.

2.3. Preparation of the CoFe-P/NF

The as-prepared CoFe-LDH/NF was put on the upper of the crucible; NaH₂PO₂·H₂O was placed on the lower layer and separated by carbon felt. The CoFe-P/NF was prepared by the solid-phase reaction between CoFe-LDH/NF and NaH₂PO₂·H₂O in an atmosphere of nitrogen (N₂). With heating rate of 3 °C/min, the temperature was raised to 350 °C and kept for 2 h. After natural cooling, the resultant CoFe-P/NF electrode was washed with DI water for a couple of times to remove the residual reactant coated, followed by drying at 50 °C in an oven. CoFe-P samples were labeled as CoFe-P-1, CoFe-P-2, and CoFe-P-4, respectively. The Co-P was prepared with the same process.

2.4. Preparation of Pt sheet and RuO₂

Pt sheet was obtained directly from CH Instruments and the area of Pt sheet is 1 cm². RuO₂ catalysts were prepared by dissolved 10 mg 20% RuO₂ into 2 mL solution of 120 μL 5% Nafion solution, 0.8 mL DI water and 1.08 mL ethanol. The homogeneous catalyst solution was obtained by ultrasonicated the mixture for 20 min. Subsequently, 50 μL of the solution was added dropwise onto the Ni foam for 4 times by using a micro sampler. Finally, dried in an oven for follow-up test.

2.5. Characterization

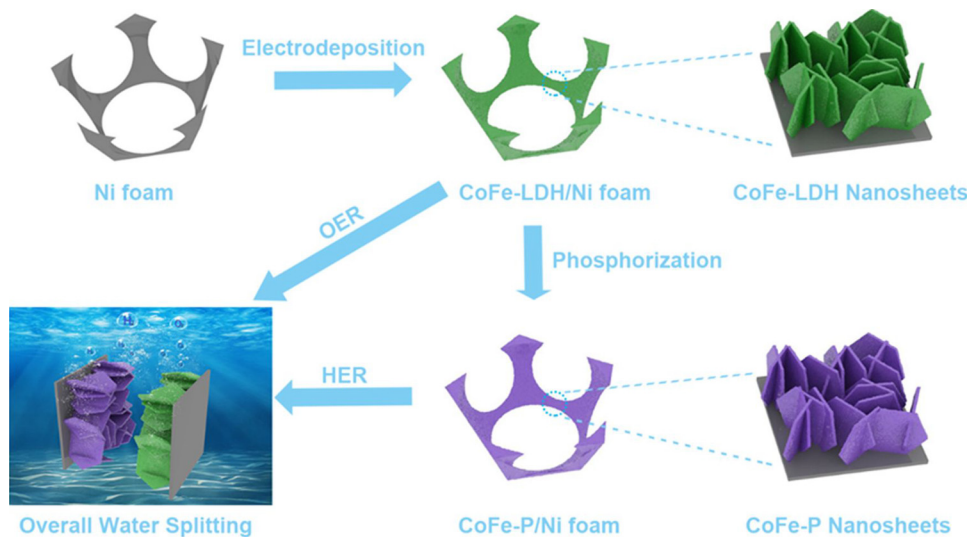
Field-emission scanning electron microscopy (FESEM, Tescan, Maia3 XMH) was used to observe the surface morphology. The element mapping was characterized by energy dispersive spectrometer (EDS, Bruker, XFlash660). X-ray diffraction (XRD) patterns analysis were carried on the Bruker D8 Advance X-ray diffractometer (Cu K α radiation). The elemental state was investigated by X-ray photoelectron spectroscopy (XPS) (IncaX-max50, Oxford). Transmission electron microscopy (TEM) images and selected-area electron diffraction (SAED) pattern were obtained on a JEOL 2010. Nanomaterial processing by using focused ion beam technology (FIB, Helios G4 CX).

2.6. Electrochemistry measurement

Electrochemical experiments were performed in a standard three-electrode system on CHI 660e electrochemical workstation. The working electrode was the as-prepared samples, a saturated calomel electrode purchased from CH Instruments was used as reference electrode and graphite rod was applied as counter electrode at the mean time. The potential values in this work are all relative to standard hydrogen electrode (vs. RHE). The potential is calibrated by adding $0.242 \pm 0.059 \times \text{pH}$ at the test potential. iR compensation within the electrolyte was used to correct the polarization curves. iR drop was compensated at 85% for OER and at 95% for HER. Linear sweep voltammetry (LSV) was applied to characterize the performance of HER and OER. LSV was carried out in 1 M KOH with a scan rate of 2 mV s⁻¹. EIS was performed in constant potential mode in the frequency range from 100 kHz to 0.01 Hz.

2.7. DFT calculation

The CASTEP code were used to perform the DFT calculation in the Materials Studio 17.1 package [68]. We approximated the exchange-correlation potential by employed the Perdew–Burke–Ernzerhof (PBE) functional and select Grimme scheme for semi-empirical dispersion correction [69,70]. The ion-electron interaction were modelled by Ultrasoft pseudopotential (OTFG type in the code). We constructed a slab from crystal and introduced a vacuum space of 10 Å to avoid spurious



Scheme 1. Fabrication process of CoFe-LDH/NF and CoFe-P/NF electrodes and their combination for water splitting.

interactions between adjacent slabs for researching the effect of hydrogen adsorption on surface. Broyden–Fletcher–Goldfarb–Shanno scheme was used to optimize structures. Each atomic energy was set as 5.0×10^{-6} eV, maximum displacement as 5.0×10^{-4} Å and maximum force as 0.01 eV Å $^{-1}$ of the convergence tolerances. A cut-off energy of 550 eV and Monkhorst-Pack mesh k-points of $4 \times 4 \times 2$ was chosen in this work. $\Delta E_{\text{ads},\text{H}} = E_{\text{slab}+\text{H}} - E_{\text{slab}} - E_{\text{H}_2}/2$ was used to defined the formation energy of hydrogen adsorption on the surface. The Gibbs free energy ($\Delta G_{\text{ads},\text{H}}$) were calculate by $\Delta E_{\text{ads},\text{H}} + \Delta E_{\text{ZPE}} - T\Delta S_{\text{H}}$ [71,72]. In this work, the (112) of FeCoP, Co₂P and (100) of Fe₂P surface were selected for calculation.

3. Results and discussion

3.1. Compositional and structural characterization of CoFe-LDH

The inexpensive Ni foam was chosen to be the substrate because of its outstanding electrochemical performance. The CoFe-LDH and Co-H were electrodeposited on the Ni foam by the constant voltage method. We synthesized different CoFe-LDH by controlling the deposition time. The entire electrodeposition process can be successfully completed at room temperature and only takes hundreds of seconds. To measure their XRD patterns, we deposited the CoFe-LDH on Ni foil substrate as it is difficult to collect CoFe-LDH powdered samples from the Ni foam. As shown in Fig. 1a, the peaks located at 44.5°, 51.8° and 76.4° correspond to the (111), (200) and (220) of Ni, according to the JCPDS#04-0850. There are three distinctly different peaks appear at 11.2°, 33.8° and 59.0° compared to the bare Ni foil. These peaks correspond to the (003), (012) and (110) characteristic diffraction of the hydrotalcite-like layer structure, respectively [73]. The typical XRD pattern confirms the LDH structure.

XPS was employed to investigate the elemental valence states of the CoFe-LDH product. The low-resolution spectra clearly showed Co, Fe, and O elements, indicating that a bimetallic hydroxide was successfully obtained (Fig. S1, Supporting information). In Fig. 1b, the Co 2p high-resolution spectrum of the CoFe-LDH, it displays two peaks at 781 and 796.3 eV, corresponding to Co 2p_{3/2} and Co 2p_{1/2} with their satellite peaks. The Co 2p_{3/2} and Co 2p_{1/2} spin-orbit splitting value is 15.3 eV, indicating the presence of Co²⁺ and Co³⁺ states. For the Fe 2p spectrum, two prominent peaks located at 713.9 and 724.5 eV can be observed in Fig. 1c, corresponding to the characteristic peaks of Fe 2p_{3/2} and Fe 2p_{1/2}, respectively, suggesting the presence of the Fe³⁺ state. As shown in Fig. 1d, the O 1s spectrum revealed peaks at 531.1 eV that are attributed to typical hydroxyl group oxygen [74]. We also analyze the

XPS spectra by using deconvolution to see the valence difference between different samples prepared by different electrodeposition time. In the XPS spectrum of Co 2p (Fig. S2a), it is obviously that the Co ion on the surface mainly contains two valence states, Co²⁺ and Co³⁺. The ratio of Co²⁺ and Co³⁺ have changed with deposition time. The proportion of Co³⁺ ions increases gradually as the electrodeposition time increases. The relative atomic ratio of Co²⁺/Co³⁺ on the surface of the CoFe-LDHs could be obtained by comparing the area that fitted curve covered. The atomic ratio of Co²⁺/Co³⁺ of CoFe-H-1, CoFe-H-2, CoFe-H-4 is 1.009, 0.986 and 0.936, respectively. We also compared the atomic ratio of Fe²⁺/Fe³⁺ on the surface of the CoFe-LDHs as shown in Fig. S2b. The atomic ratio of Fe²⁺/Fe³⁺ of CoFe-H-1, CoFe-H-2, CoFe-H-4 is 0.971, 0.968 and 0.920, respectively. The proportion of Fe³⁺ ions also increases gradually as the electrodeposition time increases.

We further investigated the morphology of the CoFe-LDH and Co-H with SEM and TEM. By adjusting the deposition time, we prepared different CoFe-LDH samples. As shown in Fig. 2a–c, different deposition time results in different morphologies. These SEM images suggest that the nanosheets grow as the deposition time increases. When the deposition time is 100 s, the surface is covered with CoFe-LDH. However, the amount of hydroxide is small, with nanosheets stacked more loosely (Fig. 2a, d). At the deposition time of 200 s, the CoFe-LDH nanosheets further grow and cover uniformly on the surface of Ni foam (Fig. 2b, e). It is obviously that the CoFe-LDH nanosheets are stacked to form 3D porous structure. This 3D porous network structure maximized the electrochemically active surface area and offered high electrode/electrolyte interface area. As the deposition time increased, the loading of hydroxide gradually increased. At 400 s, as the increase of the hydroxide loading, the porous structure formed by nanosheets also decreased (Fig. 2c, f). In addition, the thickness of the CoFe-LDH samples were different. We used FIB to characterize the thickness of the samples and sprayed a small amount of Pt to protect the sample before processing. In Fig. 2g–i, it is obviously that the thickness increases with deposition time, thickness of CoFe-H-1, CoFe-H-2 and CoFe-H-4 is 750 nm, 945 nm and 1.54 μm, respectively. We also prepared Co-H with the same method. From Fig. S3, the morphology of Co-H is also a nanosheet structure. However, the Co-H nanosheets arrange more closely than the CoFe-LDH structure. This difference in morphology also affects their electrochemical properties. Fig. S4 shows the typical image of bare Ni foam. After deposition, the surface of Ni foam is covered with nanosheets as shown in Fig. 2j. The SEM and EDS mapping images in Fig. 2j indicate that these nanosheets are CoFe-LDH. As shown in Fig. 2k, SEM image of the cross section and element mapping can also demonstrate the nanosheets are composed of three elements, Co, Fe, O.

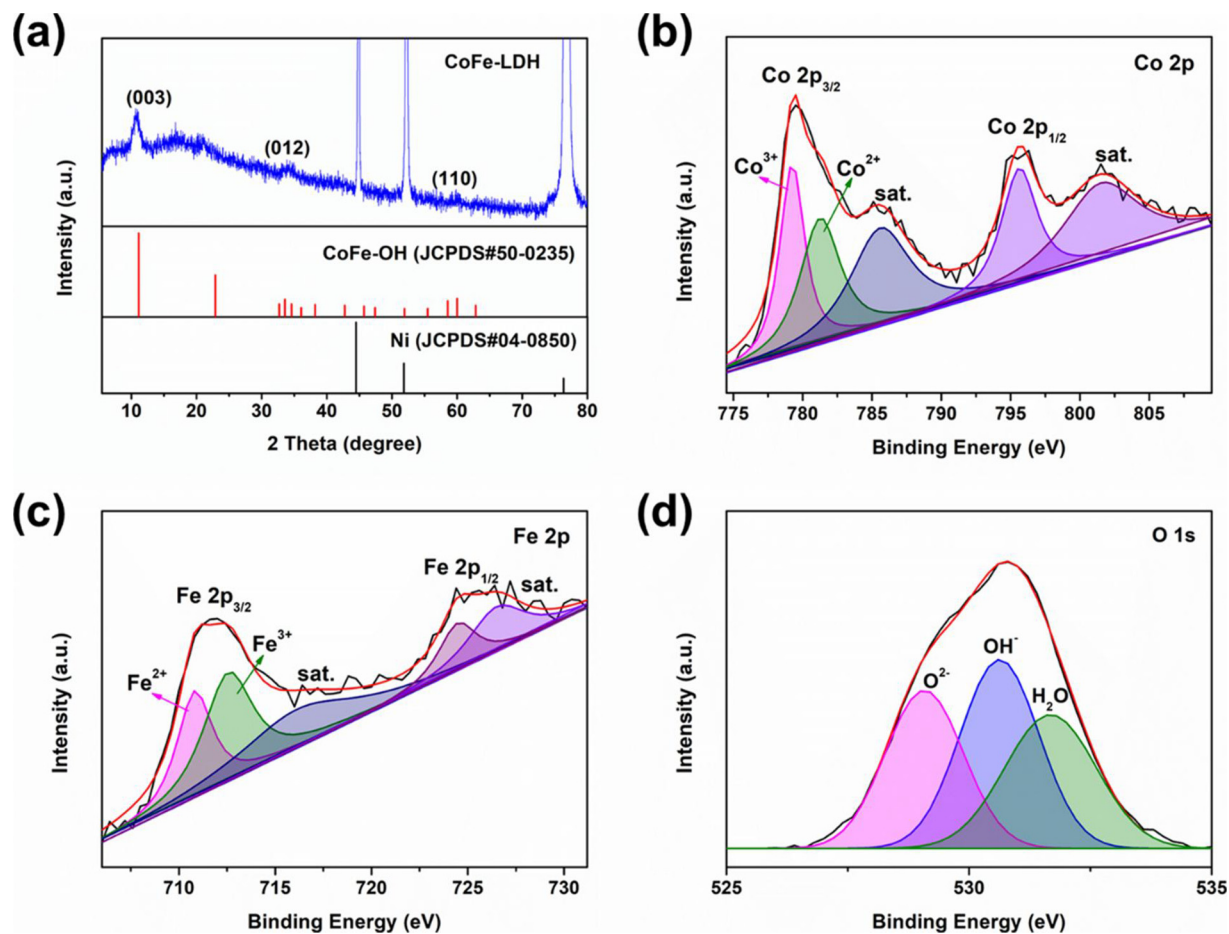


Fig. 1. (a) XRD patterns of CoFe-LDH nanosheets and the standard card of CoFe-OH, Ni. XPS spectra of (b) Co 2p, (c) Fe 2p and (d) O 1s of CoFe-H-2.

TEM and high-resolution TEM (HRTEM) images of the CoFe-LDH nanosheets (Fig. 2l, m) demonstrate that the material is a thin nanosheet with good crystallinity. The interplanar distance is measured of 0.25 nm, corresponding to the (012) plane of the LDH phase (Fig. 2m inset). The chemical elements of as-prepared LDH nanosheets are further characterized by TEM elemental mapping images. It is obviously that the elements of Co, Fe, and O are uniformly distributed in Fig. 2n.

3.2. Electrochemical activity and stability of CoFe-LDH

As the CoFe-LDH were deposited on the Ni foam successfully, the OER performance of CoFe-LDH and Co-H were investigated. The electrocatalytic activity of these CoFe-LDH nanosheet samples toward OER was evaluated in O₂-saturated alkaline solution (1 M KOH) with the as-prepared samples directly applied as working electrodes (see the Experimental Section for details). The iR-corrected polarization curves were presented, which were recorded at a low scan rate of 2 mV s⁻¹. The CoFe-LDH samples exhibit excellent catalytic activity for OER in Fig. 3a. Among these samples, the CoFe-H-2 possesses the minimal overpotential of 250 mV to reach 10 mA cm⁻². However, the RuO₂, Co-H, CoFe-H-1, CoFe-H-4 and bare NF catalysts show overpotentials of 310, 280, 270, and 360 mV, respectively (Fig. 3b). Since FeSO₄ cannot form Fe-H by electrodeposition, it can be seen from the literature that the OER performance of Fe-H is poor [51]. Therefore, its OER performance was not displayed. Tafel slopes were used to characterize the reaction kinetics for CoFe-LDH nanosheets. In Fig. 3c, the CoFe-H-2 displays the smallest Tafel slope of 35 mV dec⁻¹. Furthermore, the Tafel slopes of RuO₂, Co-H, CoFe-H-1, and CoFe-H-4 are 98, 79, 57, and 46 mV dec⁻¹, respectively. Electrochemical impedance spectroscopy (EIS) was used to investigate the charge transfer abilities as shown in

Fig. 3d. The smaller radius corresponds to the faster electron transfer kinetics of the redox reaction and lower charge transfer resistance. The arc radius of CoFe-H-2 is obviously smaller than other samples, which suggests a smaller charge transfer resistance and results in enhanced OER performance. To further understand its excellent OER performance, we calculated the electrochemical surface areas (ECSAs) of CoFe-LDH samples and Co-H from their double layer capacitance (C_{dl}) by the cyclic voltammetry method (Fig. S5). ECSAs is generally considered to be a key parameter for the high electrochemical performance. The higher ECSAs value of CoFe LDH/NF will lead to the larger active area for the enhancement of the OER performance. As shown in Fig. 3e, the C_{dl} (because C_{dl} is generally proportional to the ECSAs) of CoFe-H-2 is 1.15 m F cm⁻², which is larger than the 0.56 m F cm⁻², 0.76 m F cm⁻², 0.89 m F cm⁻² of Co-H, CoFe-H-1, CoFe-H-4, respectively. This result suggests that the possible reasons for the effect of deposition time on performance, including: (1) The increase in deposition time will significantly increase the amount of catalyst on the electrode surface. The amount of catalyst on the surface of the electrode has a great influence on its electrochemical performance. Song Jin et al. also prepared the CoFe-H by electrodeposition. They studied the OER performance of CoFe-H samples with different deposition times. They suggested that the higher catalyst loading might enhance the catalytic performance, but a higher electrocatalyst loading would suppress the charge transfer between CoFe-H and substrate, decreasing the catalytic performance of CoFe-H [51]. This is consistent with our experimental results. (2) In addition to the effect of loading, electrodeposition time also affects the valence state on the surface. The surface ions also affect the electrocatalytic performance. We compared the valence difference between different samples with different electrodeposition time by XPS spectra. From the results (Fig. S2), it is obviously that the valence states

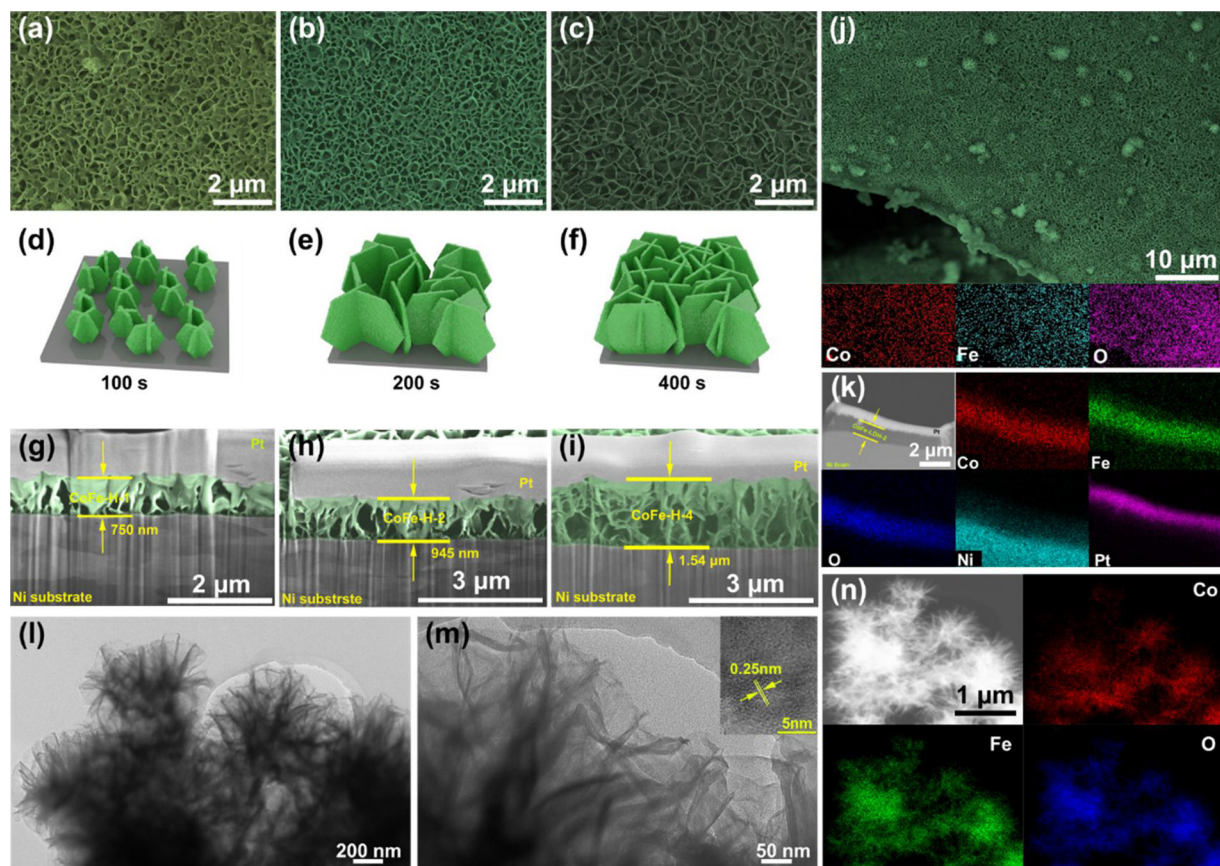


Fig. 2. SEM image of CoFe-LDH with different electrodeposition time (a) CoFe-H-1, (b) CoFe-H-2, (c) CoFe-H-4. Schematic diagram of CoFe-LDH/NF with different electrodeposition time (d) 100 s, (e) 200 s, (f) 400 s. FIB cross-sectional images of different CoFe-LDH samples (g) 100 s, (h) 200 s, (i) 400 s. (j) SEM and elemental mapping images of CoFe-LDH/NF. (k) SEM image of the cross section and element mapping. (l, m) TEM and HR-TEM images of the CoFe-LDH nanosheets, the inset is striation pattern. (n) TEM elemental mapping images of CoFe-LDH scratched off from Ni foam.

of surface Co ions mainly includes, Co^{2+} and Co^{3+} . As the deposition time increases, the proportion of Co^{3+} increases. The larger Co^{2+} ratio means better catalytic performance [31]. As the deposition time increases, although the Co^{2+} ratio decreases, but the total Co^{2+} amount is increasing. Therefore, the catalytic performance is enhanced as the deposition time increases. However, when the ratio of Co^{2+} is relatively low, the catalytic performance degrades. Therefore, when the proportion and quantity of Co^{2+} are moderate, the optimal catalytic activity is obtained. (3) It is well known that an increase in the electrochemical active surface area (ECSA) accelerates the catalytic activity of the electrode. Through the ECSA (Fig. 3e), it is obviously that the CoFe-H-2 has a larger active surface area than the CoFe-H-1, CoFe-H-4, Co-H. Moreover, the low EIS value suggests the lower charge-transfer resistance and faster electron transfer kinetics of the redox reacting. In the EIS characterization (Fig. 3d), the radius of CoFe-H-2 is smallest, that is CoFe-H-2 have the lowest EIS value. Therefore, we believed that the suitable thickness of CoFe-H-2 that creating more unsaturated metals as active sites and meanwhile improving the intrinsic electronic conductivity, which contributes to the enhancement OER activity.

For practical applications, the long-term stability of the catalyst is also very important besides the catalytic activity. The stability of the CoFe-LDH/NF electrocatalyst was tested at 10 mA cm^{-2} for 50 h. As shown in Fig. 3f, the CoFe-LDH/NF electrode exhibited long-term stability. The morphology of CoFe-LDH after OER was also characterized in Fig. 3f inset. From the SEM and EDS mapping images, it is obvious that the CoFe-LDH maintains the stability of structure. The structure stability was also very important for a catalyst. Therefore, we have characterized the CoFe-LDH catalyst after OER test by XRD, XPS and TEM images. The XRD pattern of the CoFe-LDH catalyst after OER (Fig.

S6) was almost the same as the previous XRD pattern. An identical characteristic peak appears at 11.2° , which is corresponding to the (003) of CoFe-LDH. In the XPS spectrum of the CoFe-LDH catalyst after OER (Fig. S7), the Co 2p spectra, the two main peaks at 781 and 796.3 eV, corresponding to $\text{Co} 2p_{3/2}$ and $\text{Co} 2p_{1/2}$. In the Fe 2p spectra, the two main peaks at 713.9 and 724.5 eV, which are associated with $\text{Fe} 2p_{3/2}$ and $\text{Fe} 2p_{1/2}$. The position of the main peaks are almost the same compared to the CoFe-LDH catalyst. We also characterized the CoFe-LDH catalyst after OER with HRTEM (Fig. S8). From the HRTEM images, it is obviously that the CoFe-LDH nanosheets maintain the crystal structure. The interplanar distance is measured of 0.25 nm, corresponding to the (012) plane of the LDH phase. Moreover, the elemental mapping images of TEM also indicated that the catalyst after OER was still composed of three elements, Co, Fe, O.

We believe that the excellent electrocatalytic performance of CoFe-LDH closely relate to the composition. Including: (a) synergistic effects between the metallic characters of Co and Fe, it is well known that the incorporation of Fe dramatically improves the OER activity of $\text{Co}(\text{OH})_2$ catalyst which is due to easier OH-intercalation by increasing disorder/porosity and also increases the number of defect or edge sites on the $\text{Co}(\text{OH})_2$ structure. The CoFe/NF facilitates the proton-coupled electron transfer steps by forming oxo species at lower potentials. This enhances the catalytic activity due to the potential synergistic effect of Co and Fe as cooperating active sites [75]. (b) FeOOH has a higher intrinsic OER activity than CoOOH but is an electrical insulator and is chemically unstable to dissolution under OER conditions in base. CoOOH is a good electrical conductor at OER potentials and chemically stable to dissolution. Therefore, CoOOH provides a conductive, chemically stable, and intrinsically porous/electrolyte-permeable host for Fe, which

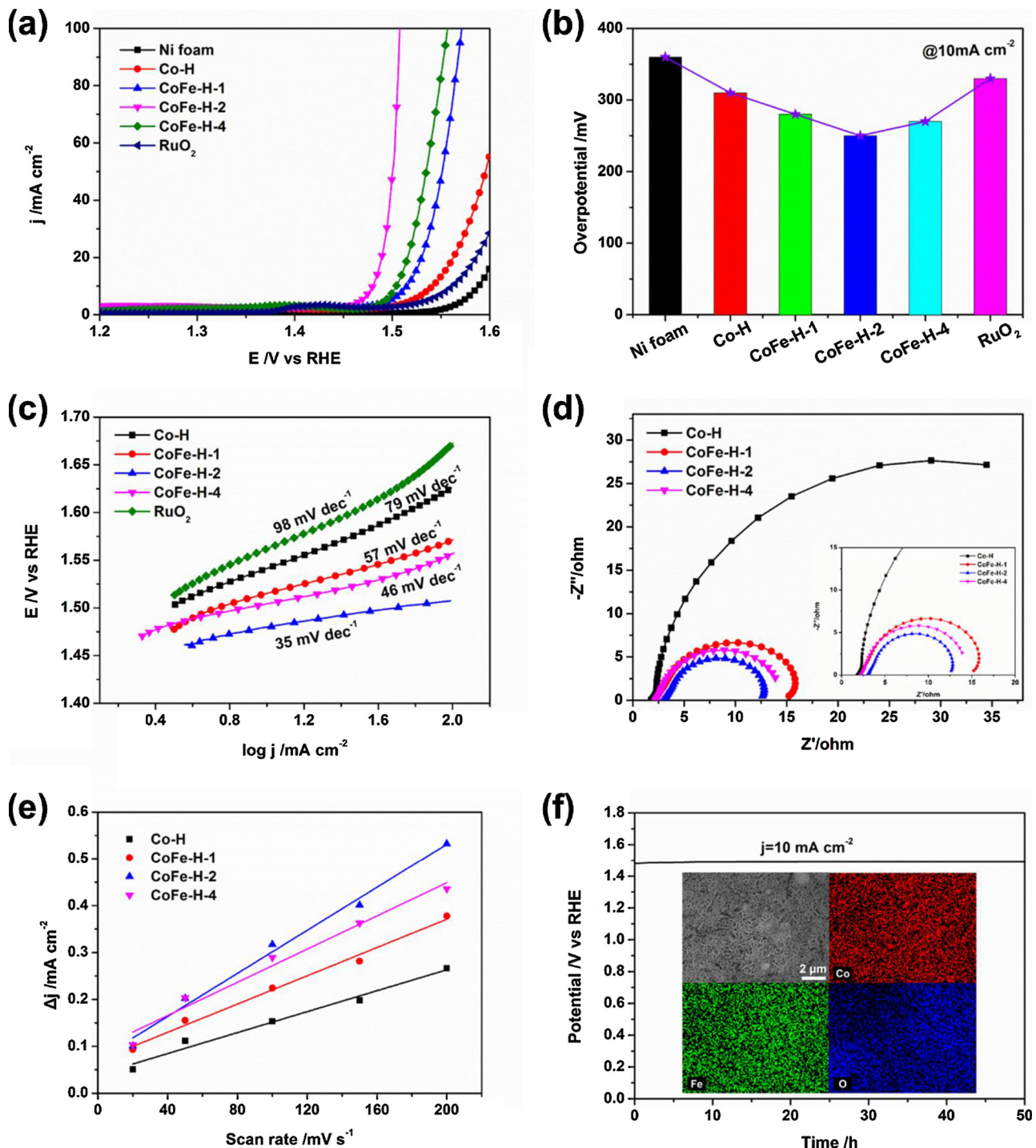


Fig. 3. (a) iR-Corrected LSV curves of various catalysts (Ni foam, Co-H, CoFe-H-1, CoFe-H-2, CoFe-H-4 and RuO_2). (b) Overpotential of different samples. (c) The corresponded Tafel plots of LSV curves. (d) Nyquist plots for Co-H, CoFe-H-1, CoFe-H-2, CoFe-H-4, the inset is a zoom-in image about the beginning part. (e) Charging current density differences (Δj) plotted against scan rates on Co-H, CoFe-H-1, CoFe-H-2, CoFe-H-4. (f) Long-term stability of CoFe-H-2 at 10 mA cm^{-2} for 50 h, the inset is SEM image and EDS mapping images of the post CoFe-H-2.

substitutes for Co and serves as the (most) active site for OER catalysis [76]. Thus, the CoFe-LDH possesses excellent activity and stability.

Compared to other different catalysts for OER (Table S1, Supporting information), it suggests that the CoFe-LDH can act as a highly efficient and stable catalyst for OER.

3.3. Structural characterization and electrochemical performance of CoFe-P

Although the CoFe-LDH exhibits great OER performance, the HER

performance remains to be improved. Herein, the bimetallic phosphide CoFe-P supported on the Ni foam was directly fabricated via a facile phosphorization process of CoFe-LDH (see details of the Experimental section). As shown in Fig. 4a, the XRD pattern of CoFe-P, the peaks located at 44.5° , 51.8° and 76.4° correspond to the (111), (200) and (220) of Ni (JCPDS#04-0850). By compared with the standard pattern of FeCoP, Co₂P and Fe₂P, as shown in Figs. 4a and S9, we find that the characteristic peaks at 40.8° , 49.0° and 74.8° correspond to the (112), (013) and (321) of FeCoP (ICSD ID: 622955) [77]. The characteristic

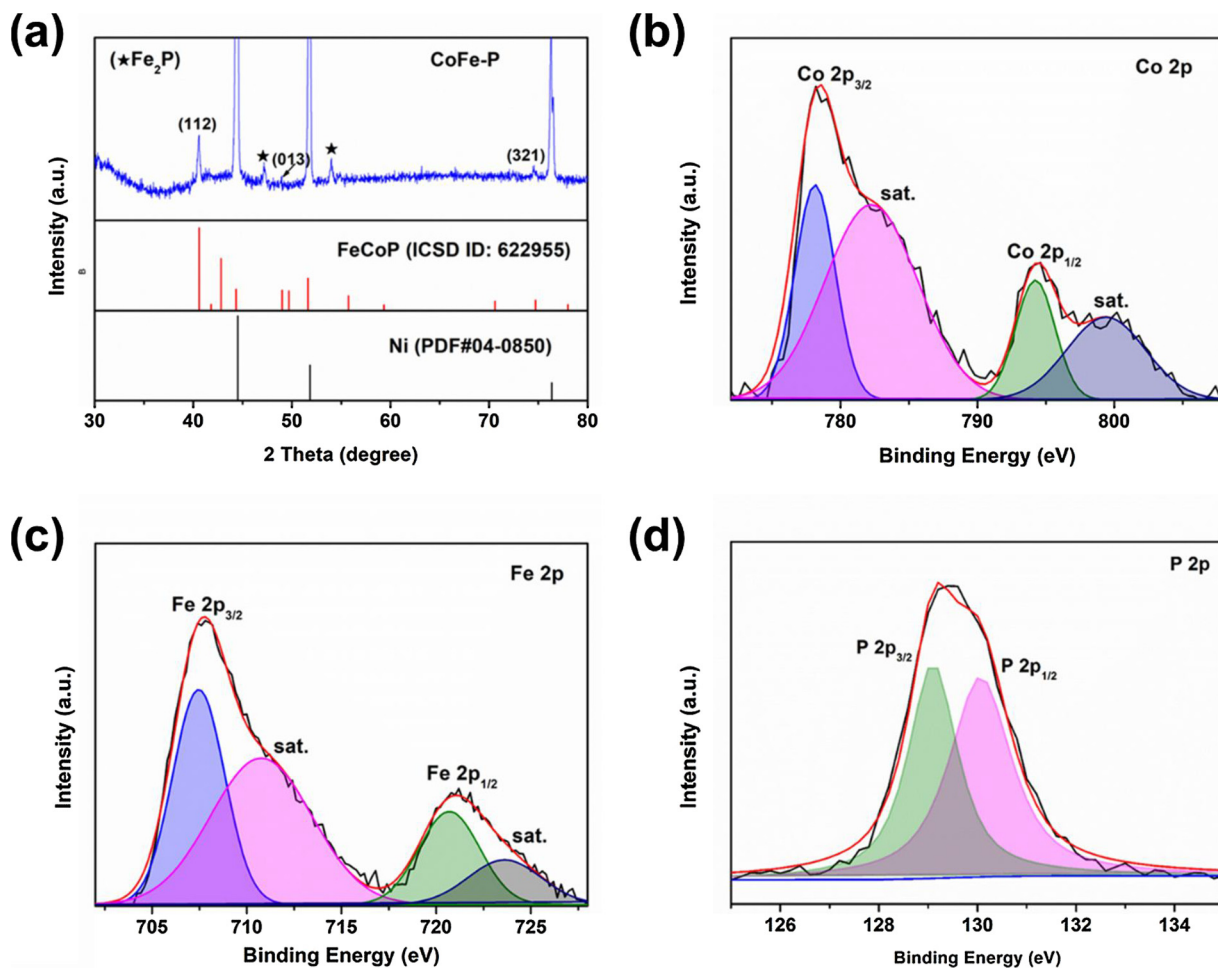


Fig. 4. (a) XRD pattern of CoFe-P and the standard card of FeCoP, Ni. XPS spectra of (b) Co 2p, (c) Fe 2p and (d) P 2p of CoFe-P.

peaks at 47.2° and 54.0° correspond to the (210) and (300) of Fe₂P [78]. In the meantime, the XRD pattern of CoFe-P is similar to the Co₂P standard card. Therefore, we believe that the FeCoP formed by Fe atoms replacing some of the Co atoms in the Co₂P.

We investigated the chemical composition and valence states of the CoFe-P product by using XPS. In Fig. S10, the low-resolution XPS spectra clearly showed Co, Fe, and P elements, indicating that a bimetallic phosphide was successfully obtained. In Co 2p spectrum of the CoFe-P (Fig. 4b), the peaks at 778.5 eV and 793.5 eV are indexed to Co 2p_{3/2} and Co 2p_{1/2}. In Fe 2p high-resolution spectrum (Fig. 4c), the peaks at 708.2 eV and 721.0 eV reflecting the binding energies of Fe 2p_{3/2} and Fe 2p_{1/2}. In Fig. 4d, the P 2p spectrum revealed peaks at 129.6 and 130.5 eV, can be attributed to the P 2p_{1/2} and P 2p_{3/2}, respectively [77]. The O 1s wide spectrum consisted of two peaks at 531.9, and 533.4 eV, which were attributed to $-\text{PO}_x$ (or P–O), C–O species (Fig. S11). The PO_x and P–O species could be generated from surface oxidation [79]. We also compared the XPS spectra of Co 2p and Fe 2p for CoFe-LDH and CoFe-P. In the Co 2p spectra of CoFe-LDH (Fig. S12a), the two main peaks at 781 and 796.3 eV, corresponding to Co 2p_{3/2} and Co 2p_{1/2}. In the Fe 2p spectra of CoFe-LDH (Fig. S12b), the two main peaks at 713.9 and 724.5 eV, which are associated with Fe 2p_{3/2} and Fe 2p_{1/2}. After the phosphating reaction, the position of the peaks are shifted. In the Co 2p spectra of CoFe-P, the two main peaks at 778.5 eV and 793.5 eV corresponding to Co 2p_{3/2} and Co 2p_{1/2}. In the Fe 2p spectra of CoFe-P, the two main peaks at 708.2 and 721.0 eV, which are associated with Fe 2p_{3/2} and Fe 2p_{1/2}.

The morphology of CoFe-H-2 after phosphorization appears nearly unchanged as shown in Fig. 5a. The element distribution with EDS

mapping was also been studied. From Fig. S13, it is obvious that the Co, Fe and P elements are uniformly covered on the NF. The CoFe-P-1, CoFe-P-4 and Co-P also retained the original morphology with the exception that the surface of nanosheets becomes rougher. (Figs. S14 and S15) The morphology of CoFe-P-2 nanosheets was further demonstrated by TEM images. From Fig. 5b, c, the TEM images of CoFe-P-2 exhibits a clear nanosheet structure, consistent with the SEM images. The HRTEM image in Fig. 5c inset demonstrates fringe spacing of 0.22 nm in certain domains, which match the spacing of (112) lattice plane of FeCoP. The fringe spacing of 0.19 nm and 0.17 nm match the spacing of (210) and (300) lattice plane of Fe₂P [77,78]. In Fig. 5d, the TEM-EDS mapping image recorded from the nanosheets shows that Co, Fe, and P elements are distributed uniformly.

As we had successfully synthesized the CoFe-P, the HER performance of CoFe-P and Co-P were studied. The electrocatalytic activity of these CoFe-P nanosheets samples toward HER was evaluated in 1 M KOH with the as-prepared samples on NF directly used as working electrodes. After phosphorization, the CoFe-P/NF electrode displayed remarkably enhanced catalytic performance. In Fig. 5e, the CoFe-P-2 exhibits superior catalytic activity toward the HER. The CoFe-P-2 sample just requires an overpotential (η) as low as 58 mV to reach a catalytic current density of 10 mA cm^{-2} , which is much lower than Ni foam (215 mV), CoFe-H-2 (199 mV) and Co-P (102 mV) at the same current density. The catalytic activity of CoFe-P-2 is even slightly better than Pt sheet (81 mV). Different phosphide also represented various electrochemical performance. In Fig. S16a, the overpotential of CoFe-P-2 is smaller than that of CoFe-P-1 (103 mV) and CoFe-P-4 (83 mV). Tafel slopes were used to characterize the reaction kinetics for CoFe-P

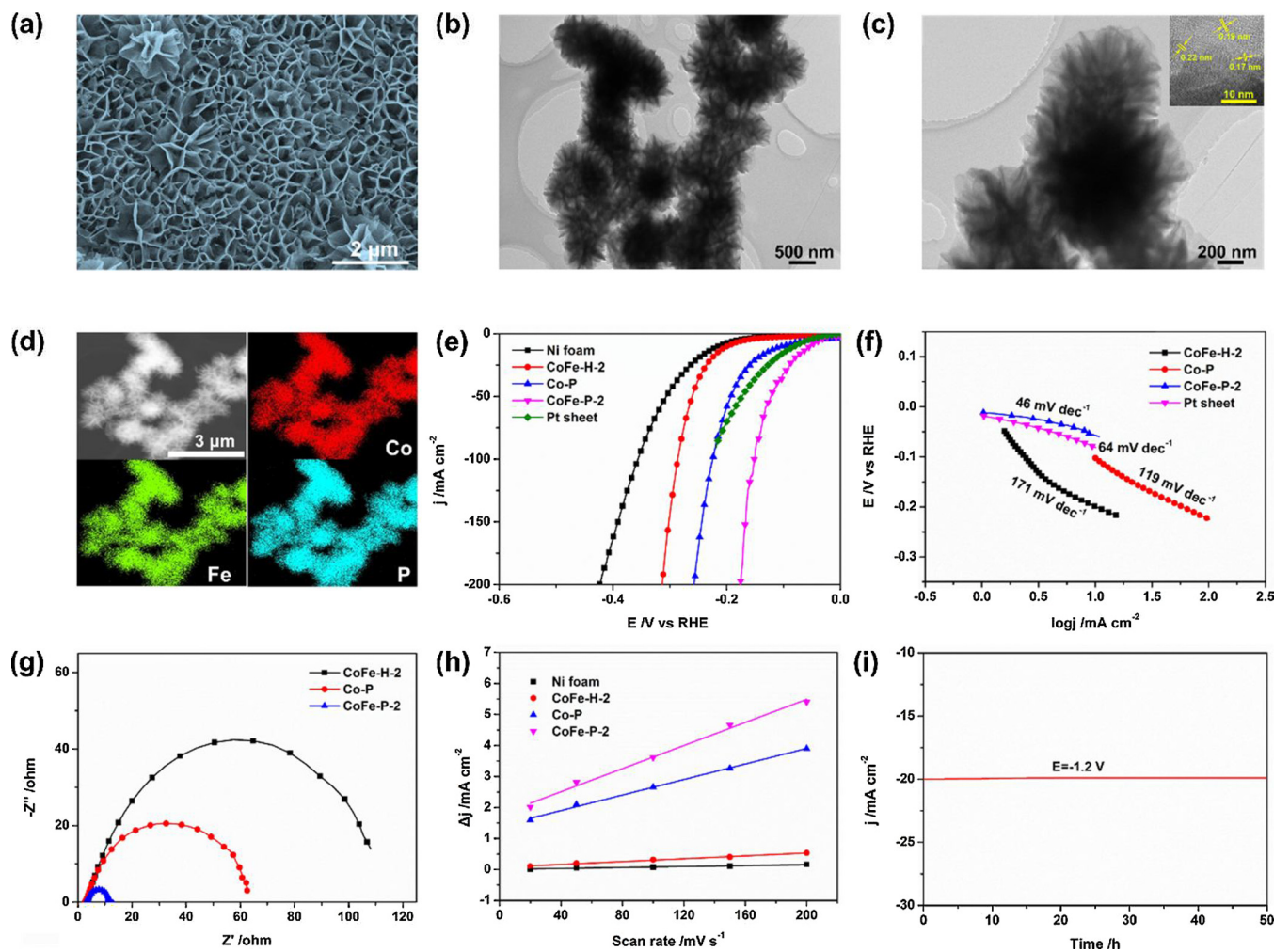


Fig. 5. (a) SEM image of CoFe-P. (b) TEM and (c) HRTEM images of CoFe-P nanosheets, inset is striation pattern. (d) TEM-EDS mapping images of the CoFe-P nanosheets. (e) iR-Corrected polarization curves of various catalysts (Ni foam, CoFe-H-2, Co-P, CoFe-P-2, and Pt sheet). (f) The corresponded Tafel plots of OER polarization curves (CoFe-H-2, Co-P, CoFe-P-2, and Pt sheet). (g) Nyquist plots for the CoFe-H-2, Co-P, CoFe-H-P. (h) Charging current density differences (ΔJ) plotted against scan rates on the Ni foam, CoFe-H-2, Co-P, CoFe-P-2. (i) Long-term stability of CoFe-P-2 at a potential of -1.2 V for 50 h.

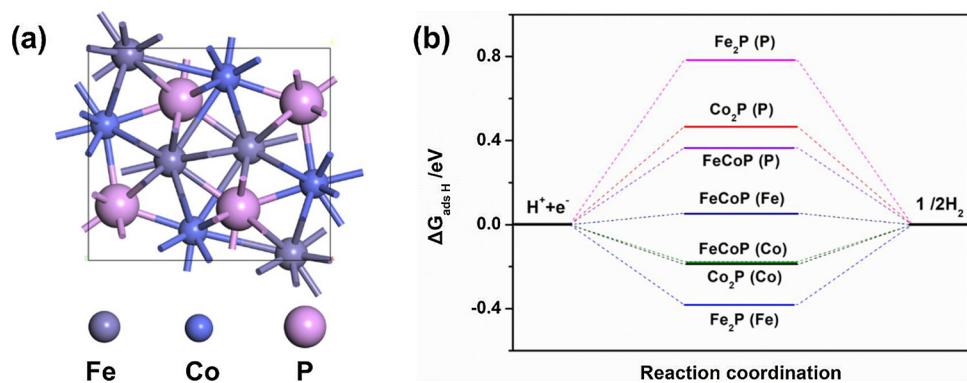


Fig. 6. (a) The slab model of FeCoP with the adsorbed hydrogen atom. (b) DFT calculation of the hydrogen adsorption energy of FeCoP, Co_2P and Fe_2P , on Co, Fe, P sites.

nanosheets. In Fig. 5f, the CoFe-P-2 shows the smallest Tafel slope of 46 mV dec^{-1} . Meanwhile, Tafel slopes of CoFe-H-2, Co-P, CoFe-P-1, CoFe-P-4 (Fig. S16b) and Pt sheet are 171 , 119 , 136 , 98 and 64 mV dec^{-1} , respectively. EIS was applied to investigate the charge transfer kinetics as shown in Fig. 5g. The smaller radius corresponding to the faster electron transfer of the redox reaction and lower charge transfer resistance. The arc radius of CoFe-P-2 is obviously smaller than other

samples, which indicates a smaller charge transfer resistance and leads to enhance HER performances. To further understand its excellent HER performance, we calculated the ECSAs of CoFe-P samples and Co-P from their double-layer capacitance (C_{dl}) by the cyclic voltammetry method (Fig. S17). The higher ECSA value, the larger active area for the enhancement of the HER performance will be. As shown in Fig. 5h, the C_{dl} (because C_{dl} is generally proportional to the ECSA) of CoFe-P-2 is

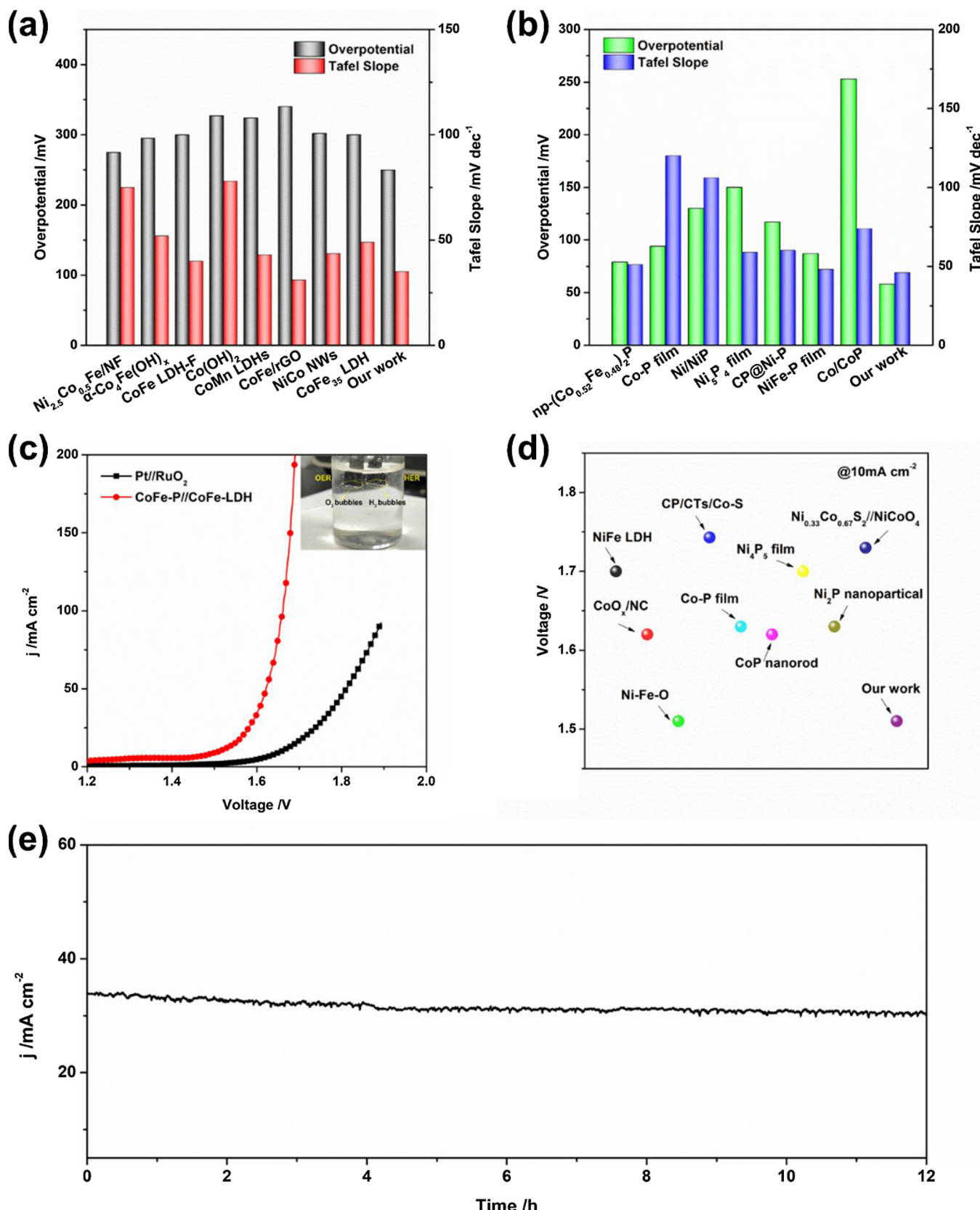


Fig. 7. (a) Comparison of different catalysts for OER and (b) catalysts for HER. (c) LSV of the CoFe-P/CoFe-LDH and Pt sheet/RuO₂ electrodes. Inset is electrolysis water device with CoFe-P/CoFe-LDH electrodes. (d) Comparison of electrocatalysts for overall water splitting in basic. (e) Long-term stability of CoFe-P/CoFe-LDH electrodes at a potential of 1.6 V for 12 h.

9.32 m F cm⁻², which is larger than the 0.38 m F cm⁻², 1.15 m F cm⁻², 6.27 m F cm⁻² of Ni foam, CoFe-H-2 and Co-P respectively. The CoFe-P/NF electrode also exhibits high durability during the HER. We tested the stability of the CoFe-P/NF electrocatalyst at a potential of -1.2 V for 50 h in 1 M KOH solution. As shown in Fig. 5i, the CoFe-P/NF electrodes exhibited negligible catalytic degradation.

We also characterized the CoFe-P catalyst after HER by XRD, XPS and TEM. The XRD pattern of the CoFe-P catalyst after HER was consistent with the previous XRD pattern (Fig. S18). The characteristic peak appears at 40.8° is corresponding to the (112) of FeCoP. The diffraction peaks at 47.2° , 54.0° are corresponding to (210), (300) in the Fe₂P phase. In the XPS spectrum of the CoFe-P catalyst after HER, in Co 2p spectrum of the CoFe-P (Fig. S19a), the peaks at 778.5 eV is indexed to Co 2p_{3/2}, the peak at 793.5 eV is indexed to Co 2p_{1/2}. In Fe 2p high-resolution spectrum (Fig. S19b), the peaks at 707.2 eV and 720.0 eV reflecting the binding energies of Fe 2p_{3/2} and Fe 2p_{1/2}. We also characterized the catalyst after HER with HRTEM (Fig. S20). From the HRTEM images, it is obviously that the CoFe-P nanosheets maintain the crystal structure. The interplanar distance is measured of 0.22 nm, corresponding to the (112) plane of the FeCoP phase. Moreover, the elemental mapping images of TEM also indicated that the catalyst after HER was still composed of three elements, Co, Fe, P.

From Table S2 (Supporting information), we can see obviously that CoFe-P-2 represents the state-of-the-art level.

3.4. DFT calculation of CoFe-P and the overall water splitting

Hydrogen adsorption free energy (ΔG_{adsH}) is an important parameter for characterizing electrocatalysts. To further understand the excellent performance of CoFe-P catalyst, we calculated the ΔG_{adsH} of CoFe-P by density functional theory (DFT) [77]. We built the model of CoFe-P according to the XRD (Fig. 6a) and calculated the values of ΔG_{adsH} on the metal sites and phosphide sites for FeCoP, Co₂P and Fe₂P. As shown in Fig. S21, we performed DFT calculation on the (112) of FeCoP and Co₂P corresponding to the highest characteristic peak in XRD pattern. The (100) surfaces of Fe₂P was reported to be the most thermal stable faces and six-layer (100) slabs with the outmost layer allowed to relax were used in our calculation [77]. In Fig. 6b, the ΔG_{adsH} of FeCoP on Co site, Fe site and P site are -0.176 eV , 0.054 eV and 0.365 eV , respectively. The ΔG_{adsH} of Co₂P on Co site and P site are -0.189 eV and 0.465 eV . The ΔG_{adsH} of Fe₂P on Fe site and P site are -0.380 eV and 0.782 eV . Among these sites, the ΔG_{adsH} of FeCoP (Fe) site the closest to thermoneutrality ($\Delta G_{\text{adsH}} = 0$). Therefore, FeCoP (Fe) sites contribute relatively more to system performance. Moreover, the $|\Delta G_{\text{adsH}}|$ of other sites of FeCoP is lower than the same sites of Co₂P and Fe₂P. As is known to all, the ΔG_{adsH} is closer to thermoneutrality, the greater the current density is attained. Therefore, based on DFT calculations, we believe that the excellent performance of the CoFe-P catalyst can due to the lowest adsorption energy. In addition to low hydrogen adsorption energy, the small impedance and large electrochemical active area are all contribute to the superior catalytic activity.

By comparing with different catalysts for OER (Fig. 7a) and HER (Fig. 7b), it is obvious that the CoFe-LDH and CoFe-P exhibit high catalytic performance. We built an alkaline electrolyzer for overall water splitting using CoFe-LDH/NF as the anode and CoFe-P/NF as the cathode, respectively. Fig. 7c shows the LSV curves of the CoFe-P/CoFe-LDH and Pt sheet/RuO₂ electrodes in 1 M KOH solution. Compared to Pt sheet/RuO₂ electrodes, the CoFe-P/CoFe-LDH electrodes have advanced catalytic performance. The voltage is as low as 1.51 V to reach the current density of 10 mA cm^{-2} , much lower than the 1.65 V of Pt sheet/RuO₂ electrodes. During the test, it was noticed that bubbles generated on the surface of the electrode (Fig. 7c inset). Compared to other electrocatalysts for overall water splitting in basic, as shown in Fig. 7d and Table S3, our catalysts are at an outstanding position. We also investigated the stability of the electrodes in 1 M KOH solution. In Fig. 7e, there is no apparent decrease in current density after long-term

stability. These results suggest that the CoFe-P/CoFe-LDH electrodes can be used as a high activity and stable catalyst for overall water splitting.

4. Conclusion

In summary, we have synthesized a 3D hierarchically structured CoFe-based electrode material with excellent catalytic performance. CoFe-LDH was prepared both as a catalytic material and as a framework by a facile electrodeposition method. This 3D porous structure makes the CoFe-LDH/NF electrode exhibit high catalytic and durability for OER. Furthermore, the CoFe-LDH electrode could be converted to the corresponding CoFe-P electrode by phosphorization. This hierarchical structured CoFe-P exhibits impressive catalytic performances for HER. In an alkaline solution, the catalytic properties of CoFe-P can be comparable to platinum. Therefore, the CoFe-P and CoFe-LDH can serve as efficient electrode materials in electrolyzer for overall water splitting. This work provides a simple but effective approach to fabricating cost-effective and high-performance electrocatalysts that can meet the scientific and societal demands for water splitting.

Appendix A. Supplementary data

Supplementary material related to this article can be found, in the online version, at doi:<https://doi.org/10.1016/j.apcatb.2018.11.091>.

References

- [1] S. Chu, A. Majumdar, *Nature* 488 (2012) 294.
- [2] C.G. Morales-Guio, L.-A. Stern, X. Hu, *Chem. Soc. Rev.* 43 (2014) 6555–6569.
- [3] M.G. Walter, E.L. Warren, J.R. McKone, S.W. Boettcher, Q. Mi, E.A. Santori, N.S. Lewis, *Chem. Rev.* 110 (2010) 6446–6473.
- [4] J. Duan, S. Chen, M. Jaroniec, S.Z. Qiao, *ACS Catal.* 5 (2015) 5207–5234.
- [5] C.F. Tan, S.A.B. Azmansah, H. Zhu, Q.-H. Xu, G.W. Ho, *Adv. Mater.* 29 (2017) 1604417.
- [6] M.-Q. Yang, Y.-J. Xu, W. Lu, K. Zeng, H. Zhu, Q.-H. Xu, G.W. Ho, *Nat. Commun.* 8 (2017) 14224.
- [7] M. Sun, G. Zhang, H. Liu, Y. Liu, J. Li, *Sci. China Mater.* 58 (2015) 683–692.
- [8] T.R. Cook, D.K. Dogutan, S.Y. Reece, Y. Surendranath, T.S. Teets, D.G. Nocera, *Chem. Rev.* 110 (2010) 6474–6502.
- [9] N.S. Lewis, D.G. Nocera, *Proc. Natl. Acad. Sci. U. S. A.* 103 (2006) 15729–15735.
- [10] M.S. Dresselhaus, I.L. Thomas, *Nature* 414 (2001) 332–337.
- [11] M.W. Kanan, D.G. Nocera, *Science* 321 (2008) 1072–1075.
- [12] J. Luo, J.H. Im, M.T. Mayer, M. Schreier, M.K. Nazeeruddin, N.G. Park, S.D. Tilley, H.J. Fan, M. Gratzel, *Science* 345 (2014) 1593–1596.
- [13] S. Park, Y. Shao, J. Liu, Y. Wang, *Energy Environ. Sci.* 5 (2012) 9331–9344.
- [14] X. Zou, Y. Zhang, *Chem. Soc. Rev.* 44 (2015) 5148–5180.
- [15] Y. Lee, J. Suntivich, K.J. May, E.E. Perry, Y. Shao-Horn, *J. Phys. Chem. Lett.* 3 (2012) 399–404.
- [16] T. Reier, M. Oezaslan, P. Strasser, *ACS Catal.* 2 (2012) 1765–1772.
- [17] E. Antolini, *ACS Catal.* 4 (2014) 1426–1440.
- [18] N. Danilovic, R. Subbaraman, K.C. Chang, S.H. Chang, Y. Kang, J. Snyder, A.P. Paulikas, D. Strmcnik, Y.T. Kim, D. Myers, V.R. Stamenkovic, N.M. Markovic, *Angew. Chem. Int. Ed.* 53 (2014) 14016–14021.
- [19] H.-S. Oh, H.N. Nong, T. Reier, M. Gliech, P. Strasser, *Chem. Sci.* 6 (2015) 3321–3328.
- [20] J. Tian, Q. Liu, A.M. Asiri, X. Sun, *J. Am. Chem. Soc.* 136 (2014) 7587–7590.
- [21] M.P. Browne, H. Nolan, G.S. Duesberg, P.E. Colavita, M.E. Lyons, *ACS Catal.* 6 (2016) 2408–2415.
- [22] F. Wang, S.Y. Song, K. Li, J.Q. Li, J. Pan, S. Yao, X. Ge, J. Feng, X. Wang, H.J. Zhang, *Adv. Mater.* 28 (2016) 10679–10683.
- [23] J.R. McKone, B.F. Sadtler, C.A. Werlang, N.S. Lewis, H.B. Gray, *ACS Catal.* 3 (2013) 166–169.
- [24] (a) J. Zhang, T. Wang, D. Pohl, B. Rellinghaus, R. Dong, S. Liu, X. Zhuang, X. Feng, *Angew. Chem. Int. Ed.* 55 (2016) 6702–6707;
(b) J. Song, H. Zhao, R. Sun, X. Li, D. Sun, *Energy Environ. Sci.* 10 (2017) 225–235;
(c) J. Zhang, T. Wang, P. Liu, S. Liu, R. Dong, X. Zhuang, M. Chen, X. Feng, *Energy Environ. Sci.* 9 (2016) 2789–2793;
(d) G. Li, Z. Du, Q. Qiao, Y. Yu, D. Peterson, A. Zafar, R. Kumar, S. Curtarolo, F. Hunte, S. Shannon, *J. Am. Chem. Soc.* 138 (2016) 16632–16638;
(e) Y. Wu, Y. Liu, G.-D. Li, X. Zou, X. Lian, D. Wang, L. Sun, T. Asefa, X. Zou, *Nano Energy* 35 (2017) 161–170.
- [25] (a) H. Wang, H.-W. Lee, Y. Deng, Z. Lu, P.-C. Hsu, Y. Liu, D. Lin, Y. Cui, *Nat. Commun.* 6 (2015) 7261;
(b) H. Schaefer, D.M. Chevrier, K. Küpper, P. Zhang, J. Wollschlaeger, D. Daum, M. Steinhart, C. Hess, U. Krupp, K. Müllerbuschbaum, *Energy Environ. Sci.* 9 (2016) 2609–2622;

(c) H.Y. Wang, S.F. Hung, H.Y. Chen, T.S. Chan, H.M. Chen, B. Liu, *J. Am. Chem. Soc.* 138 (2015) 36–39;

(d) M. Huynh, C. Shi, S.J. Billinge, D.G. Nocera, *J. Am. Chem. Soc.* 137 (2015) 14887–14904.

[26] (a) B. Zhang, C. Xiao, S. Xie, J. Liang, X. Chen, Y. Tang, *Chem. Mater.* 28 (2016) 6934–6941;

(b) Y. Zhang, B. Ouyang, J. Xu, G. Jia, S. Chen, R.S. Rawat, H.J. Fan, *Angew. Chem. Int. Ed.* 55 (2016) 8670–8674;

(c) P. Chen, K. Xu, Y. Tong, X. Li, S. Tao, Z. Fang, W. Chu, X. Wu, C. Wu, *Inorg. Chem. Front.* 3 (2016) 236–242.

[27] (a) M. Ledendecker, S. Krick Calderón, C. Papp, H.-P. Steinrück, M. Antonietti, M. Shalom, *Angew. Chem. Int. Ed.* 127 (2015) 12538;

(b) B. You, N. Jiang, M. Sheng, S. Gul, J. Yano, Y. Sun, *Chem. Mater.* 27 (2015) 7636–7642;

(c) H. Liang, A.N. Gandi, D.H. Anjum, X. Wang, U. Schwingenschlögl, H.N. Alshareef, *Nano Lett.* 16 (2016) 7718–7725.

[28] X. Zhu, C. Tang, H.F. Wang, B.Q. Li, Q. Zhang, C. Li, C. Yang, F. Wei, *J. Mater. Chem. A* 4 (2016) 7245–7250.

[29] A.L. Wang, H. Xu, G.R. Li, *ACS Energy Lett.* 1 (2016) 445–453.

[30] H. Jin, S. Mao, G. Zhan, F. Xu, X. Bao, Y. Wang, *J. Mater. Chem. A* 5 (2017) 1078–1084.

[31] P.F. Liu, S. Yang, B. Zhang, H.G. Yang, *ACS Appl. Mater. Interfaces* 8 (2016) 34474–34481.

[32] Y. Tong, J. Xu, H. Jiang, F. Gao, Q. Lu, *Chem. Eng. J.* 316 (2017) 225–231.

[33] H. Jin, J. Wang, D. Su, Z. Wei, Z. Pang, Y. Wang, *J. Am. Chem. Soc.* 137 (2015) 2688–2694.

[34] F. Song, X. Hu, *J. Am. Chem. Soc.* 136 (2014) 16481–16484.

[35] J.-X. Feng, H. Xu, Y.-T. Dong, X.-F. Lu, Y.-X. Tong, G.-R. Li, *Angew. Chem. Int. Ed.* 56 (2017) 2960–2964.

[36] J.-X. Feng, J.-Q. Wu, Y.-X. Tong, G.-R. Li, *J. Am. Chem. Soc.* 140 (2018) 610–617.

[37] A.-L. Wang, H. Xu, G.-R. Li, *ACS Energy Lett.* 1 (2016) 445–453.

[38] C. You, Y. Ji, Z. Liu, X. Xiong, X. Sun, *ACS Sustain. Chem. Eng.* 6 (2018) 1527–1531.

[39] D. Liu, Q. Lu, Y. Luo, X. Sun, A.M. Asiri, *Nanoscale* 7 (2015) 15122–15126.

[40] X. Xu, F. Song, X. Hu, *Nat. Commun.* 7 (2016) 12324.

[41] X. Gao, H. Zhang, Q. Li, X. Yu, Z. Hong, X. Zhang, C. Liang, Z. Lin, *Angew. Chem. Int. Ed.* 55 (2016) 14693–14697.

[42] K. Yan, G.S. Wu, W. Jin, *Energy Technol.* 4 (2016) 354–368.

[43] S. Chen, J. Duan, M. Jaroniec, S.Z. Qiao, *Angew. Chem. Int. Ed.* 52 (2013) 13567–13570.

[44] J.X. Feng, H. Xu, Y.T. Dong, S.H. Ye, Y.X. Tong, G.R. Li, *Angew. Chem. Int. Ed.* 55 (2016) 3694–3698.

[45] J. Wang, W. Cui, Q. Liu, Z. Xing, A.M. Asiri, X. Sun, *Adv. Mater.* 28 (2016) 215–230.

[46] Y. Wu, M. Chen, Y. Han, H. Luo, X. Su, M.T. Zhang, X. Lin, J. Sun, L. Wang, L. Deng, W. Zhang, R. Cao, *Angew. Chem. Int. Ed.* 54 (2015) 4870–4875.

[47] J.-X. Feng, H. Xu, Y.-T. Dong, S.-H. Ye, Y.-X. Tong, G.-R. Li, *Angew. Chem. Int. Ed.* 55 (2016) 3694–3698.

[48] T. Zhang, J. Du, P. Xi, C.L. Xu, *ACS Appl. Mater. Interfaces* 9 (2017) 362–370.

[49] X. Han, C. Yu, J. Yang, C. Zhao, H. Huang, Z. Liu, P.M. Ajayan, J. Qiu, *Adv. Mater. Interfaces* 3 (2016) 1500782.

[50] Y. Zhang, Q. Shao, Y. Pi, J. Guo, X. Huang, *Small* 13 (2017) 1700355.

[51] W. Liu, H. Liu, L. Dang, H. Zhang, X. Wu, B. Yang, Z. Li, X. Zhang, L. Lei, S. Jin, *Adv. Funct. Mater.* 27 (2017) 1603904.

[52] S. Han, Y. Feng, F. Zhang, C. Yang, Z. Yao, W. Zhao, F. Qiu, L. Yang, Y. Yao, X. Zhuang, X. Feng, *Adv. Funct. Mater.* 25 (2015) 3899–3906.

[53] P. Jiang, Q. Liu, Y. Liang, J. Tian, A.M. Asiri, X. Sun, *Angew. Chem. Int. Ed.* 53 (2014) 12855–12859.

[54] E.J. Popczun, C.G. Read, C.W. Roske, N.S. Lewis, R.E. Schaak, *Angew. Chem. Int. Ed.* 53 (2014) 5427–5430.

[55] Q. Liu, J. Tian, W. Cui, P. Jiang, N. Cheng, A.M. Asiri, X. Sun, *Angew. Chem. Int. Ed.* 53 (2014) 6710–6714.

[56] E.J. Popczun, J.R. McKone, C.G. Read, A.J. Biacchi, A.M. Wiltrot, N.S. Lewis, R.E. Schaak, *J. Am. Chem. Soc.* 135 (2013) 9267–9270.

[57] J. Tian, Q. Liu, N. Cheng, A.M. Asiri, X. Sun, *Angew. Chem. Int. Ed.* 53 (2014) 9577–9581.

[58] P. Xiao, M.A. Sk, L. Thia, X. Ge, R.J. Lim, J. Wang, K.H. Lim, X. Wang, *Energy Environ. Sci.* 7 (2014) 2624–2629.

[59] Z. Xing, Q. Liu, A.M. Asiri, X. Sun, *Adv. Mater.* 26 (2014) 5702–5707.

[60] J. Chang, L. Liang, C. Li, M. Wang, J. Ge, C. Liu, W. Xing, *Green Chem.* 18 (2016) 2287–2295.

[61] J.-X. Feng, S.-Y. Tong, Y.-X. Tong, G.-R. Li, *J. Am. Chem. Soc.* 140 (2018) 5118–5126.

[62] M. Sun, H. Liu, J. Qu, J. Li, *Adv. Energy Mater.* 6 (2016) 1600087.

[63] G. Zhang, G. Wang, Y. Liu, H. Liu, J. Qu, J. Li, *J. Am. Chem. Soc.* 138 (2016) 14686–14693.

[64] S. Li, G. Zhang, X. Tu, J. Li, *ChemElectroChem* 5 (2018) 701–707.

[65] Y. Li, H. Zhang, M. Jiang, Q. Zhang, P. He, X. Sun, *Adv. Funct. Mater.* 27 (2017) 1702513.

[66] C. Wu, Y. Yang, D. Dong, Y. Zhang, J. Li, *Small* 13 (2017) 1602873.

[67] Y. Feng, X.-Y. Yu, U. Paik, *Chem. Commun.* 52 (2016) 1633–1636.

[68] S. Clark, M. Segall, C. Pickard, P. Hasnip, M. Probert, K. Refson, M. Payne, Z. Kristallogr. Cryst. Mater. 220 (2005) 567.

[69] J. Perdew, K. Burke, M. Ernzerhof, *Phys. Rev. Lett.* 77 (1996) 3865.

[70] S. Grimme, *J. Comput. Chem.* 27 (2006) 1787–1799.

[71] H. Pan, *Sci. Rep.* 4 (2014) 5348.

[72] B. Hinnemann, P. Moses, J. Bonde, K. Jorgensen, J. Nielsen, S. Horch, I. Chorkendorff, J. Nørskov, *J. Am. Chem. Soc.* 127 (2005) 5308–5309.

[73] S.J. Kim, Y. Lee, D.K. Lee, J.W. Lee, J.K. Kang, *J. Mater. Chem. A* 2 (2014) 4136–4139.

[74] P. Babar, A. Lokhande, H.H. Shin, B. Pawar, M.G. Gang, S. Pawar, J.H. Kim, *Small* 14 (2018) 1702568.

[75] F. Yang, K. Sliozberg, I. Sinev, H. Antoni, A. Bahr, K. Ollegott, W. Xia, J. Masa, W. Grenert, B. Roldan Cuenya, W. Schuhmann, M. Muhler, *ChemSusChem* 10 (2017) 156–165.

[76] M.S. Burke, M.G. Kast, L. Trotochaud, A.M. Smith, S.W. Boettcher, *J. Am. Chem. Soc.* 137 (2015) 3638–3648.

[77] J. Kibsgaard, C. Tsai, K. Chan, J.D. Benck, J.K. Nørskov, F. Abild-Pedersen, T.F. Jaramillo, *Energy Environ. Sci.* 8 (2015) 3022–3029.

[78] X. Zhang, S. Zhu, L. Xia, C. Si, F. Qu, F.L. Qu, *Chem. Commun.* 54 (2018) 1201–1204.

[79] Y. Yang, X. Liang, F. Li, S. Li, X. Li, S. Ng, C.-M.L. Wu, R. Li, *ChemSusChem* 11 (2018) 376–388.